

Microring Electrodes: A Computational Study of Transport-Limited Processes

Benjamin A. Brookes,[†] David J. Gavaghan,[‡] and Richard G. Compton^{*,†}

Physical and Theoretical Chemistry Laboratory, Oxford University, South Parks Road, Oxford OX1 3QZ, United Kingdom, and Oxford University Computing Laboratory, Wolfson Building, Oxford University, Parks Road, Oxford OX1 3QZ, United Kingdom

Received: November 2, 2001; In Final Form: January 24, 2002

Investigations at microring electrodes are limited by the lack of equations that describe short and long time behavior at rings of all thicknesses. In this paper, a robust finite difference numerical method is presented for the simulation of electrochemical processes at microring electrodes of intermediate thickness. The method relies on a careful meshing strategy to minimize electrode flux errors. The accuracy of the method is first tested by comparison with a well-established reversible steady-state analytical equation. The meshes obtained through this process are reused to produce current results for chronoamperometry and linear-sweep voltammetry. In the case of chronoamperometry, simulated currents show less than $\pm 1.5\%$ difference compared to integral-equation methods. In the case of linear-sweep voltammetry, currents are recorded across nine decades of dimensionless scan rate. Both the dimensionless peak current and voltage at half-peak height are compared with other known methods and shown to be either comparable to or better than alternative results. In the case of the voltage at half-peak height, results are confirmed by simulations at the microdisk electrode.

1. Introduction

Microring electrodes have received significant attention^{1–6} recently because of their increasingly wide range of experimental applications. This is primarily because the large perimeter-to-area (PAR) ratio results in enhanced current density providing an ideal geometry for kinetic measurements. Because the limiting geometries of zero and infinite interior radius (corresponding to microdisk and microband electrodes, respectively) exhibit such dissimilar transient and steady-state behavior, a full theoretical description of the microring response poses a challenging problem. To date such investigations have been based around analytical or semianalytical approaches. Closed analytical expressions for the electrode current have been published by several authors in the “thin ring” limit,^{7–11} following the work of Smythe.¹² The majority of these methods implement a constant flux approximation at the electrode surface. Results that do not use this assumption have been presented recently in work by Philips et al.,¹³ Tallman et al., and Wu et al. Tallman reports the most complete set of results using an integral-equation method,¹⁴ and details data for chronoamperometry,¹⁵ linear-sweep voltammetry,¹⁶ and even square-wave voltammetry experiments.¹⁷ However, to the authors’ best knowledge, no purely numerical methods or results have been published for electrodes of this geometry despite the attractiveness of such an approach in terms of the ready extension to systems of realistic experimental conditions. In this paper, we accordingly present a general, robust method for the simulation of steady-state, chronoamperometric, and linear-sweep experiments at ring electrodes of intermediate thickness. These will employ a method of flux error minimization, explored by Gavaghan¹⁸ for the case of the microdisk electrode, with

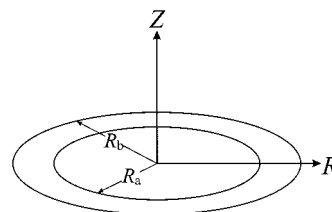


Figure 1. Diagram illustrating the geometry of the microring problem.

the aims of producing reliable results for geometric and temporal domains for which the thin-ring analytical theory has yet to attain reliable results. The results will be compared to existing analytical solutions, and where appropriate, their failures will be indicated. In subsequent papers we intend to illustrate how the flexibility of the numerical method will allow results to be gathered and analysis to be made of more complex reactions under experimental investigation.

2. Theory for the Transport-Limited Steady-State Experiment

2.1. Deriving a Suitable Mesh for Transport-Limited Steady-State Voltammetry. The steady-state diffusion-only mass transport of a single species A is given in normalized cylindrical polar coordinates as

$$D_A \left\{ \frac{\partial^2 [A]}{\partial Z^2} + \frac{\partial^2 [A]}{\partial R^2} + \frac{1}{R} \frac{\partial [A]}{\partial R} \right\} = 0 \quad (1)$$

where D_A is the diffusion coefficient of A and Z and R are the distances normal to and radial to the electrode surface. Figure 1 illustrates the geometry of the problem. We characterize the ring electrode with the inner and outer radii, R_a and R_b , respectively. To simplify numerical solutions, we nondimen-

* To whom correspondence should be sent.

[†] Physical and Theoretical Chemistry Laboratory.

[‡] Oxford University Computing Laboratory.

sionalize all spatial variables with respect to the outer electrode radius, R_b :

$$\frac{Z}{R_b} = z; \quad \frac{R}{R_b} = r; \quad \frac{R_a}{R_b} = r_a \quad (2)$$

so at $R = R_a$, $r = r_a$, and $R = R_b$, $r = 1$.

Mass transport eq 1 may now be rewritten as

$$\frac{\partial^2 a}{\partial r^2} + \frac{\partial^2 a}{\partial z^2} + \frac{1}{r} \frac{\partial a}{\partial r} = 0 \quad (3)$$

where $a = [A]/[A]_{\text{bulk}}$ and $[A]_{\text{bulk}}$ is the bulk concentration of A. We investigate a transport-limited reductive process:



at the surface of the electrode. A solution to eq 3 is sought with the following boundary conditions:

$$\begin{aligned} r > 0; \quad z \rightarrow \infty; \quad a &= 1 \\ r > 1; \quad z = 0; \quad \frac{\partial a}{\partial z} &= 0 \\ r < r_a; \quad z = 0; \quad \frac{\partial a}{\partial z} &= 0 \\ r = 0; \quad z \geq 0; \quad \frac{\partial a}{\partial r} &= 0 \\ r \rightarrow \infty; \quad z \geq 0; \quad a &= 1 \end{aligned} \quad (5)$$

We assume that species A is totally consumed at the electrode surface; thus,

$$1 \geq r \geq r_a; \quad z = 0; \quad a = 0 \quad (6)$$

The resulting current is defined as

$$I = 2\pi R_b F D_A [A]_{\text{bulk}} \int_{r_a}^1 \left(\frac{\partial a}{\partial z} \right)_{z=0} r \, dr \quad (7)$$

It is also convenient to consider the dimensionless current, ψ :

$$\psi = \frac{\pi}{2} \int_{r_a}^1 \left(\frac{\partial a}{\partial z} \right)_{z=0} r \, dr \quad (8)$$

In all numerical solutions, we will replace the infinite solution space $[0, \infty) \times [0, \infty)$ with the finite region $[0, r_{\text{max}}] \times [0, z_{\text{max}}]$. The values of z_{max} and r_{max} will be chosen to be sufficiently large that they do not affect the current at the electrode surface.

To gain an appreciation of the difficulties in solving the problem defined above, we consider the similar microdisk steady-state problem, for which the analytical solution is known.¹⁹ A selection of numerical methods^{20–22} have been used to produce results on regular meshes. These have all yielded poor spatial convergence unless very fine meshes are used. Gavaghan¹⁸ used solutions on a square mesh in cylindrical polar coordinates to show that the error in the flux, ψ , in the element inside and adjacent to the electrode insulator boundary interface (a “boundary singularity”) varies as approximately $0.54h^{1/2}$ where h is the radial width of the element. Also, errors in the flux from the remaining elements on the inner part of the electrode are generally opposite in sign. Thus, by expanding the spacings in the mesh away from the singularity, a mesh may be generated to yield very accurate steady-state current compared to the known analytical solution. Moreover, the

method allows a prediction of the upper error bound of the accuracy of the electrode current prediction as the solution moves away from steady-state conditions.

In the microring electrode, an extra boundary discontinuity is present on the interior of the ring. Despite the fact that the exact concentration distribution around both interior and exterior discontinuities will differ to that in the microdisk, if the flux errors are distributed in a similar manner, error canceling may be possible. Unfortunately, for the microring electrode, we are unable to undertake a rigorous treatment because of the lack of an exact analytical solution for the steady-state current and, in particular, the electrode flux. The accepted exact solution for the microring current may have been found by analogy with the theory formulated by Smythe¹² on the capacitance of the circular annulus:

$$I = nFD[A]_{\text{bulk}} l_0 \quad (9)$$

where

$$(l_0)_{\text{exact}} = \frac{\pi^2(R_a + R_b)}{\ln \left[16 \left(\frac{R_b + R_a}{R_b - R_a} \right) \right]} \quad \text{where} \quad (R_b - R_a)/R_b \ll 1 \quad (10)$$

Several authors have provided alternative approximate equations to predict the steady-state current as a function of ring thickness. While most are again accurate only in the thin-ring limit, an empirical equation by Szabo predicts the current across the whole range of r_a , from microdisk ($r_a = 0$) to thin ring ($r_a \rightarrow 1$). Szabo's approximate version of eq 10 is reformulated as

$$(l_0)_{\text{empirical}} = \frac{\pi^2(R_a + R_b)}{\ln \left[\left(\frac{32R_a}{R_b - R_a} \right) + \exp \left(\frac{\pi^2}{4} \right) \right]} \quad (11)$$

Tallman states that the equation is accurate to 0.2% for intermediate rings,²³ and also in the thin-ring limit agrees with other exact solutions.¹² Thus, for the purposes of the work presented here, eq 9 is sufficiently accurate to allow optimization of a mesh on which accurate “steady-state” calculations may be performed. The extra singularity in the ring electrode will increase computational demands, in comparison to the microdisk electrode, if accuracy is to be maintained. Also, unlike the microdisk problem, we cannot directly probe how the flux errors vary with mesh spacings around these two singularities because no exact analytical equation exists. Nevertheless, it has been proven by Whiteman et al.²⁴ that for mixed boundary value problems of this type increasing mesh refinement will always result in convergent behavior. Thus, it should always be possible to devise a mesh that predicts a current to a given tolerance of the value using eq 11. If a suitable mesh is generated that accurately simulates the transport-limited steady-state problem, it may be reused for solving other voltammetric problems at ring electrodes of the same thickness.

Our chosen method requires the mesh to expand geometrically away from both the ring electrode inner edge ($z = 0$; $r = r_a$) and the ring electrode outer edge ($z = 0$; $r = 1$). To simplify the description of the mesh, we define regions in the R (R_1 , R_2 , R_3 and R_4) and Z (Z_1) coordinates where mesh spacings increase geometrically in either a positive or negative axis direction. If the direction of expansion is positive, then the mesh spacings increase as they move to positive axis positions. Where the number of nodes in a particular region is nonintegral, the last

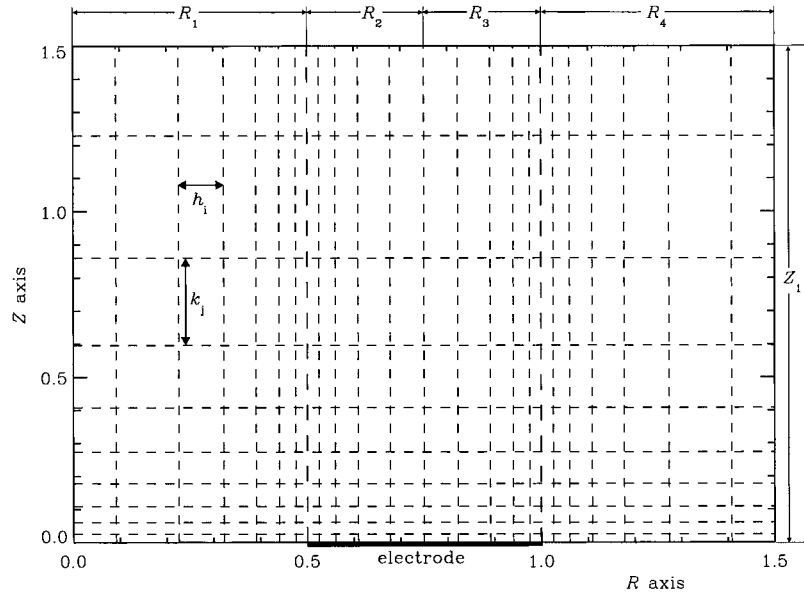


Figure 2. Section of a discretization mesh generated with the parameter values $h_{\text{last}} = 5 \times 10^{-1}$ and $f = 1.40$.

(largest) spacing is truncated to fit the remaining space. All meshes used in this approach may therefore be described by the system given in Table 1. In all simulations detailed in this work, the expansion factor, f , by which the mesh spacings increase or decrease in a particular grid domain, and the initial mesh spacing in a particular region, h_{last} , which defines the sizes of elements adjacent to both electrode discontinuities, are kept constant for analytical convenience. Consequently, any mesh (with specified values of r_{max} and z_{max}) may be fully characterized by the expansion factor, f , and the initial mesh separation at the annulus, h_{last} . Table 1 provides sufficient information to generate a mesh of nodes at locations (r_i, z_j) where

$$i = 0, 1, 2, \dots, n$$

$$j = 0, 1, 2, \dots, m$$

on which discretization may be performed. Nodes with i or j indices of zero are located on the R and Z axes, respectively. The mesh spacings h_i and k_j are defined as

$$\begin{aligned} h_i &= r_{i+1} - r_i & i &= 0, 1, \dots, n-1 \\ k_j &= z_{j+1} - z_j & j &= 0, 1, \dots, m-1 \end{aligned} \quad (12)$$

An example mesh for parameter values $f = 1.4$ and $h_{\text{last}} = 0.1$ is illustrated in Figure 2. We seek an approximate solution vector, \mathbf{u} , to the exact concentration solution $a(r_i, z_j)$ at each point on the mesh. The element in the vector \mathbf{u} for a species at a location (r_i, z_j) is denoted U_{ij} . The finite difference formulation of the differential operators may be derived from Taylor expansions (see appendix of ref 18).

$$\begin{aligned} a_{rr} &\approx \frac{2(h_{i-1}U_{i+1,j} - (h_{i+1} + h_i)U_{i,j} + h_iU_{i-1,j})}{h_{i-1}h_i(h_i + h_{i-1})} \\ a_r &\approx \frac{(h_{i-1}^2U_{i+1,j} - (h_{i-1}^2 - h_i^2)U_{i,j} - h_i^2U_{i-1,j})}{h_{i-1}h_i(h_i + h_{i-1})} \\ a_{zz} &\approx \frac{2(k_{j-1}U_{i,j+1} - (k_{j+1} + k_j)U_{i,j} + k_jU_{i,j-1})}{k_{j-1}k_j(k_j + k_{j-1})} \end{aligned} \quad (13)$$

TABLE 1: Description of the General Meshing Technique Used in All Ring Simulations

region	start	finish	direction of expansion
Z_1	$z = 0$	$z = z_{\text{max}}$	positive
R_1	$r = 0$	$r = r_a$	negative
R_2	$r = r_a$	$r = (r_a + r_b)/2$	positive
R_3	$r = (r_a + r_b)/2$	$r = r_b$	negative
R_4	$r = r_b$	$r = r_{\text{max}}$	positive

2.2. Boundary Conditions. At the cylindrically symmetric z axis, we make use of the MacLaurin expansion to modify u_r :

$$\frac{1}{r}a_r = a_{rr} \quad \text{at } r = 0 \quad (14)$$

Thus, mass transport eq 3 becomes

$$0 = a_{zz} + 2a_{rr} \quad (15)$$

We impose Neumann boundary conditions by assigning fictitious concentration values outside the simulation domain. For the axis of symmetry,

$$U_{-1,j} = U_{1,j} \quad \text{and} \quad h_{-1} = h_0 \quad (16)$$

and therefore, we obtain the central finite difference equality:

$$2a_{rr} = \frac{4(U_{1,j} - U_{0,j})}{h_0^2} \quad (17)$$

At the insulating surround, we use a one-sided second-order Taylor expansion to describe the flux:

$$a_z \approx -\left(\frac{k_0^2 U_{i,2} - (k_0 + k_1)^2 U_{i,1} + k_1(k_1 + 2k_0)U_{i,0}}{k_0 k_1 (k_1 + k_0)} \right) \quad (18)$$

Equation 18 can be used to isolate a value for $U_{i,0}$ at the insulating surround as well as evaluate the flux at the electrode surface. The finite difference formulas given in eq 13 combined with the relevant boundary conditions above define a set of

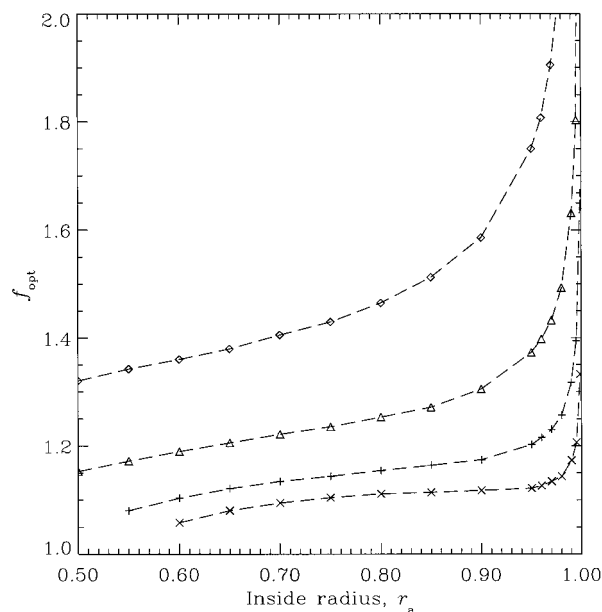


Figure 3. Optimized values of f in the error minimization algorithm for mesh with values of h_{last} of 10^{-3} (\diamond), 10^{-4} (Δ), 10^{-5} ($+$), and 10^{-6} (\times).

linear of equations, which may be recast in vector matrix form as

$$\mathbf{M} \cdot \mathbf{u} = \mathbf{d} \quad (19)$$

where \mathbf{u} is a vector of unknown concentrations of length $2n(m-1)$, \mathbf{M} is a sparse matrix of size $2n(m-1) \times 2n(m-1)$, and \mathbf{d} is a known vector of length $2n(m-1)$. Equation 19 was solved using the BICGSTAB iterative solver from the F11 NAG FORTRAN library, which has been shown to be particularly appropriate for electrochemical problems.²⁵

3. Steady-State Results and Discussion

A binary search algorithm was written to minimize the difference between solutions of eq 3 and solution of eq 9 with $l_0 = (l_0)_{\text{empirical}}$. The expansion factor at which this occurs is labeled f_{opt} . Successive iterations were performed until the difference in the dimensionless current was less than 10^{-4} . Results were collected for values of $h_{\text{last}} = 10^{-3}$, 10^{-4} , 10^{-5} , and 10^{-6} across the range of microring thicknesses of $r_a = 0.05$ – 0.999 . In all cases, the values of r_{max} and z_{max} were set to 1000, which was shown to be sufficiently far that doubling the values had no noticeable effect on the current; halving r_{max} and z_{max} from 1000 to 500 resulted in a change of ψ of less than 5×10^{-4} . The resulting values of f_{opt} are illustrated in Figure 3 and tabulated in Table 2. Omitted data in Table 2 was the result of the low expansion factors necessary for optimization leading to unfeasibly fine meshes, which could not be solved in reasonable CPU time. Rings thinner than $r_a = 0.999$ would typically lead to solver failure. As can be seen, accurate simulations of transport-limited steady-state currents are achievable for most ring thicknesses on meshes of varying coarseness. For all values of h_{last} , f_{opt} increases exponentially as the ring becomes increasingly thin. Moreover, the smaller the values of h_{last} are, the thinner the ring has to be before significant increases in f_{opt} are observed. It is apparent that the most accurate results will be gained for meshes where f_{opt} varies little with r_a because the mesh accuracy will be most tolerant to changes in the concentration profile. This variation is smallest for the finer meshes, and therefore, within the restrictions of CPU time, the finest meshes should be used for transient experiments. It is

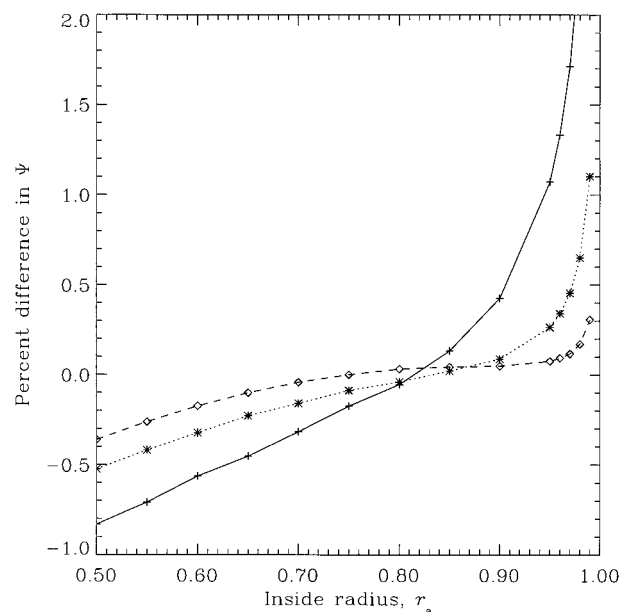


Figure 4. Diagram of the percent difference in ψ compared to eq 11 on meshes of 10^{-4} ($+$), 10^{-5} ($*$), and 10^{-6} (\diamond) with $f = 1.09$, 1.15 , 1.25 , respectively.

TABLE 2: Optimal Expansion Factors, f , for a Variety of Ring Thickness, γ , and Initial Mesh Spacings, h_{last}

r_a	h_{last}			
	10^{-3}	10^{-4}	10^{-5}	10^{-6}
0.10	1.224			
0.20	1.221			
0.30	1.247			
0.40	1.284	1.103		
0.50	1.320	1.153		
0.60	1.360	1.190	1.103	1.058
0.70	1.405	1.221	1.134	1.095
0.80	1.465	1.253	1.155	1.112
0.90	1.586	1.305	1.174	1.118
0.95	1.750	1.373	1.202	1.122
0.96	1.807	1.398	1.216	1.127
0.97	1.905	1.433	1.230	1.134
0.98	2.066	1.493	1.257	1.144
0.99	2.433	1.631	1.317	1.173
0.995	3.077	1.803	1.395	1.206
0.999	7.878	2.549	1.668	1.333

convenient to select one value of f_{opt} for each value of h_{last} , because this allows the method to be justified as “general” to all ring thicknesses. Because, for the meshes in which $h_{\text{last}} = 10^{-4}$, 10^{-5} , and 10^{-6} , f_{opt} generally increases slowly for $r_a < 0.95$, an approximate averaged value of f_{opt} between $r_a = 0.5$ and 0.95 is chosen on which to perform further simulations. The values are $f = 1.09$, 1.15 , and 1.25 for $h_{\text{last}} = 10^{-4}$, 10^{-5} , and 10^{-6} , respectively. Steady-state simulations were therefore run with these three meshes to see how the percentage error in the dimensionless current ψ varies with the inside ring radius, r_a . The results as shown in Figure 4 illustrate that for the $h_{\text{last}} = 10^{-5}$ and 10^{-6} meshes we obtain good steady-state accuracy with maximum errors less than ca. $\pm 0.5\%$ in the range $r_a = 0.5$ – 0.97 . For the $h_{\text{last}} = 10^{-4}$ mesh, errors increase more rapidly but are still less than ca. $\pm 1\%$ in range of $r_a = 0.5$ – 0.95 , which was specified as the aim of the method. Having characterized three test meshes, we may now evaluate how they perform in modeling non-steady-state problems.

4. Diffusion-Limited Chronoamperometry

A general method has been derived for generating meshes on which to simulate transport-limited steady-state currents. This

method will be applied to test the performance when simulating chronoamperometric transients. The dimensionless time-dependent mass transport equation is

$$\frac{R_b^2}{D_A} \frac{\partial a}{\partial t} = \frac{\partial^2 a}{\partial z^2} + \frac{\partial^2 a}{\partial r^2} + \frac{1}{r} \frac{\partial a}{\partial r} \quad (20)$$

To improve time accuracy of the solutions, we chose a time function such that time intervals expand geometrically, that is,

$$\Delta t_m = \Delta t_0 \delta^{m-1} = t_{m+1} - t_m \quad m = 1, 2, \dots, NT$$

where t_m is the time at iteration m and δ is the time expansion factor. The time derivative of eq 20 can be expressed with a simple two-point approximation:

$$\frac{R_b^2}{D_A} \frac{\partial a}{\partial t} = \frac{R_b^2}{D_A \Delta t_m} (\mathbf{u}^{m+1} - \mathbf{u}^m) \quad (21)$$

Few workers have reported either numerical or analytical results for ring transients. Szabo reports an extended eq 9 to incorporate time dependence at long times:

$$\lim_{t \rightarrow \infty} I = I_0(1 + I_0/\sqrt{4\pi^3 D_A t}) \quad (22)$$

Szabo illustrated that eq 22 operates more generally for both microdisk ($l_0 = 4R_e$) and hemispherical ($l_0 = 2\pi R_e$) electrodes. Tallman¹⁵ uses an integral-equation method and numerically tabulated the current i_R as a function of t_R for a number of microring electrode thicknesses, which are based on the dimensionless perimeter-squared-to-area ratio, γ :

$$\gamma = \frac{1 + r_a}{2(1 - r_a)} \quad (23)$$

i_R and t_R are defined as

$$t_R = Dt/L^2; \quad i_R = I/(nFD[A]_{\text{bulk}}L)$$

where $L = R_b - R_a$ Wu et al.²⁶ used Szabo's eq 11 to derive an approximate equation of steady-state current, defined in the t_R and γ variables used by Tallman:

$$i_R(t_R) = 2\pi\gamma \left[\frac{1}{\sqrt{\pi t_R}} + \frac{H\sqrt{t_R} + \gamma + 1/2}{\sqrt{\pi t_R} + \gamma + 1/2} \right] \quad (24)$$

where H is defined in terms of γ such that

$$H = \frac{\pi^{3/2}}{\ln[32.05(\gamma - 0.13212)]} \quad (25)$$

H equates to Szabo's l_0 in eq 11 as

$$H = \sqrt{\pi} l_0 / R_b \quad (26)$$

Wu et al. state that eq 24 is applicable for “any radius of ring and at any time”. In the corresponding analysis of our results, we will consider primarily the tabulated results of Tallman for ring thicknesses of $\gamma = 1.0, 3.0$, and 10.0 because these are the most complete set of results and also Wu's analytical eq 24. Simulations were run with the same ring thicknesses (which correspond to $r_a = 1/3, 0.714$, and 0.904) in conjunction with the parameters given in Table 3. The relatively fine mesh with

TABLE 3: Parameters Values Used in the Simulation of Transients

parameter	units	simulation value
D_A	$\text{cm}^2 \text{s}^{-1}$	1×10^{-5}
$[A]_{\text{bulk}}$	mol cm^{-3}	1×10^{-6}
R_b	cm	1×10^{-3}
t_{sim}	s	10.0
E°	V	0.0
T	K	298
h_{last}		10^{-4}
f		1.25
NT		1000
δ		1.025

$h_{\text{last}} = 10^{-4}$ was chosen because of the large amount of time iterations chosen for the transient simulations. Log–log plots of the transients for all three rings along with overlaid plots of transients from solutions of eq 22 and Oldham's short-term transient equation²⁷ are shown in Figure 5a–c. Tabulated results for all three methods are shown in Table 4. Plots of the percentage difference between simulated and Tallman's integral-equation methods are plotted in Figure 6. As can be seen, all simulated results differ by not more than 1% compared to Tallman, validating the quality of both methods. In particular, the poorest agreement is for the $\gamma = 1.0$ electrode, for which the simulated results exhibit a current between 0.4% and 1.0% higher than that from Tallman's results. Simulated results for the $\gamma = 3.0$ and 10.0 electrodes however show discrepancies of less than ca. $\pm 0.4\%$. For all three ring thicknesses, there is no significant trend in errors with electrolysis time, which supports the quality of the meshing protocol. Considering that the $\gamma = 1.0$ ring is outside the range of ring thicknesses that were specified in the original aims of the meshing method, these results are encouraging. In contrast, comparison of the simulated results with Wu's equation highlights significant inaccuracies, being up to 13%, 8%, and 2% inaccurate for $\gamma = 1.0, 3.0$, and 10.0 , respectively. Because the mesh optimization method demands choosing a specific value of f , it is advantageous to test how well accuracy may be retained on meshes with higher or lower values of f . This will allow an evaluation of the robustness of the method. Figure 7 illustrates how the deviation from Tallman's results for a ring of $\gamma = 10.0$ varies with dimensionless time on meshes of different f with $h_{\text{last}} = 10^{-4}$. As can be seen, the effect of increasing f is to lower the observed current (thereby reducing the observed discrepancy). In general for this ring, the current increases by about 0.4% for an increase in f of 0.1. Increasing f from its steady-state optimum value reduces the error relative to Tallman's results. We may therefore suggest that for the mesh where $h_{\text{last}} = 10^{-4}$, if f is between 1.10 and 1.20, the errors in the dimensionless current at any time should be within $\pm 1.5\%$. Clearly, for meshes of lower h_{last} , we would expect higher accuracy with the same tolerance in f .

5. Linear-Sweep Voltammetry

We consider the simple redox couple



which possesses potential-dependent forward and backward rate constants, k_f and k_b , defined as

$$k_f = k^\circ \exp\left(-\frac{\alpha nF}{RT}[E(t) - E^\circ]\right) \quad (28)$$

$$k_b = k^\circ \exp\left(\frac{(1 - \alpha)nF}{RT}[E(t) - E^\circ]\right) \quad (29)$$

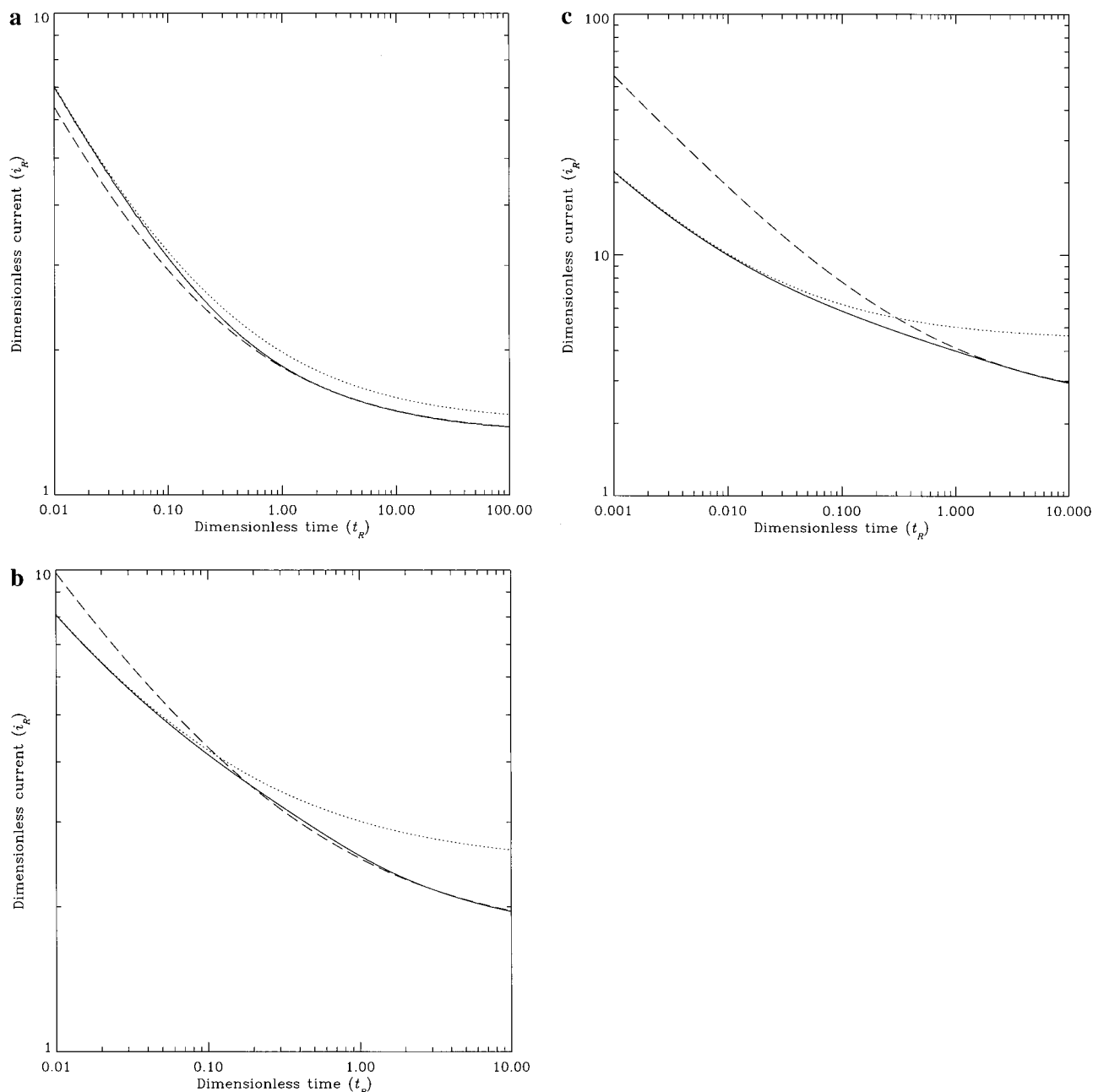


Figure 5. Log-log plots of the transients for all rings with (a) $\gamma = 1$, (b) $\gamma = 3$, and (c) $\gamma = 10$. Plots of transients from solutions of eq 22 (dashed line) and Oldham's short-time transient equation²⁶ (dotted line) are overlaid.

where $E^{\circ'}$ is the formal potential. The potential wave form in the linear-sweep voltammetry (LSV) experiment changes as

$$E(t) = E_i + vt \quad (30)$$

where E_i is the applied potential at the start of the experiment and v is the scan rate in V s^{-1} . The pertinent mass-transport equations governing the behavior of A and B are

$$\frac{R_b^2}{D_A} \frac{\partial a}{\partial t} = \frac{\partial^2 a}{\partial z^2} + \frac{\partial^2 a}{\partial r^2} + \frac{1}{r} \frac{\partial a}{\partial r} \quad (31)$$

$$\frac{R_b^2}{D_B} \frac{\partial b}{\partial t} = \frac{\partial^2 b}{\partial z^2} + \frac{\partial^2 b}{\partial r^2} + \frac{1}{r} \frac{\partial b}{\partial r} \quad (32)$$

The boundary conditions applicable to the A species at all nonelectrode boundaries are given in eq 8. Those applicable to

the B species are identical apart from those at the limits of R and Z space, where we assume no B is present in bulk solution

$$\begin{aligned} r > 0; \quad z = z_{\max}; \quad b &= 0 \\ r = r_{\max}; \quad z > 0; \quad b &= 0 \end{aligned} \quad (33)$$

Conservation of flux at the electrode surface results in the boundary conditions for species A and B being

$$D_A \frac{\partial a}{\partial z} \Big|_{z=0} = -D_B \frac{\partial b}{\partial z} \Big|_{z=0} \quad (34)$$

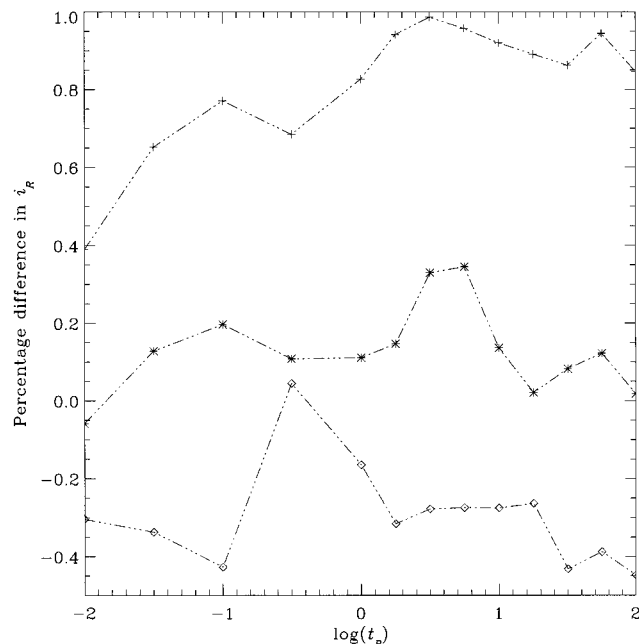
and

$$\frac{D_A}{R_b} \frac{\partial a}{\partial z} \Big|_{z=0} = k_f a_0 - k_b b_0 \quad (35)$$

where a_0 and b_0 are the surface concentrations of A and B,

TABLE 4: Comparison of i_R Results for Chronoamperometry

$\log(t_R)$	integral-equation			analytical			simulation		
	$\gamma = 1$	$\gamma = 3$	$\gamma = 10$	$\gamma = 1$	$\gamma = 3$	$\gamma = 10$	$\gamma = 1$	$\gamma = 3$	$\gamma = 10$
-2.00	41.740	125.300	417.700	41.600	124.829	416.781	41.867	125.374	416.080
-1.50	26.160	78.750	262.500	26.000	78.013	261.198	26.249	78.649	260.800
-1.00	17.300	52.490	175.000	17.151	51.409	173.222	17.374	52.387	173.661
-0.50	12.210	37.480	125.100	12.084	36.041	122.942	12.205	37.439	124.249
0.00	9.305	28.430	95.540	9.146	26.874	93.398	9.320	28.399	94.756
0.25	8.418	25.110	85.090	8.171	23.695	83.204	8.445	25.073	84.296
0.50	7.789	22.310	76.470	7.423	21.151	74.961	7.811	22.237	75.723
0.75	7.327	19.960	69.230	6.850	19.098	68.115	7.347	19.891	68.574
1.00	6.986	18.120	63.080	6.410	17.433	62.275	7.005	18.095	62.505
1.25	6.734	16.790	57.730	6.074	16.084	57.178	6.752	16.786	57.220
1.50	6.535	15.850	52.920	5.818	14.994	52.670	6.563	15.837	52.468
1.75	6.398	15.160	48.670	5.624	14.122	48.669	6.423	15.142	48.215
2.00	6.290	14.630	45.050	5.476	13.429	45.143	6.318	14.627	44.672

**Figure 6.** Diagram showing the discrepancy in i_R between the simulated transients and the tabulated data given by Tallman for rings of $\gamma = 1$ (+), 3 (*) and 10 (\diamond).

respectively. The assumption that $D_A = D_B = D$, which is common for electrochemical experiments in which oxidized and reduced species are similar, leads to the result

$$a = 1 - b \quad (36)$$

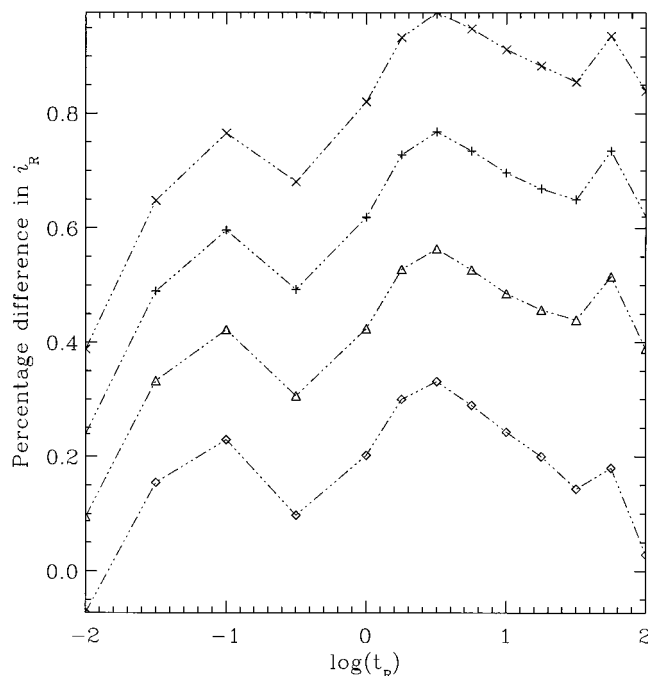
This allows the two coupled partial differential equations 31 and 32 to be reduced to a single partial differential equation. Combining eq 35 with eq 36 results in the new boundary condition

$$\frac{D_A}{R_b} \frac{\partial a}{\partial z} \Big|_{z=0} = (k_b + k_f) a_0 - k_b \quad (37)$$

Calculating the derivative $\partial a / \partial z$ using a two-point approximation results in the implicit formulation of electrode boundary condition being

$$U_{0,j} = \frac{F}{k_f + k_b + F} U_{1,j} + \frac{k_b}{k_f + k_b + F} \quad (38)$$

where $F = D/(R_b k_0)$. The electrode flux may still be calculated using a higher-order finite difference approximation by combining eqs 18 and 38. Because in the LSV experiment

**Figure 7.** Comparison of simulated microring diffusion-limited transients with integral-equation results for a microring of thickness $\gamma = 10$, $h_{\text{last}} = 10^{-4}$, and differing values of f : (x) 1.15; (+) 1.19385 (f_{opt}); (Δ) 1.25; (\diamond) 1.30.

there is no time discontinuity in species concentrations, we use a regular time interval, Δt , between solution iterations. To gain a more accurate evaluation of the concentration time derivative, it is facile to implement a Richtmyer modification²⁸ as

$$\frac{\partial a}{\partial t} = \frac{1}{\Delta t} \sum_{j=1}^{j_{\text{level}}} R_j \mathbf{u}^{m+2-j} \quad (39)$$

where R_j is a set of coefficients specific to the number of concentration values used in the approximation, j_{level} . The potential wave form was discretized such that all potential-dependent parameters were updated before solution iteration with the potential at the $m+1^{\text{th}}$ time level. Unless otherwise stated, all linear-sweep simulations are calculated with j_{level} set to 6.

6. Linear-Sweep Voltammetry Results and Discussion

Results for reversible linear-sweep voltammetry at ring electrodes have been comprehensively studied by Kalpathy et al.¹⁶ Tabulated data of peak height, I_{max} , and half-peak potential,

TABLE 5: Parameter Values Used in the Simulation of Linear-Sweep Voltammetry

parameter	units	simulation value
D_A	$\text{cm}^2 \text{s}^{-1}$	1×10^{-5}
$[A]_{\text{bulk}}$	mol cm^{-3}	1×10^{-6}
R_a	cm	1×10^{-3}
$E^{\circ'}$	V	0.0
k°	cm s^{-1}	10^{10}
E_i	V	0.3
E_f	V	-0.3
T	K	298
h_{last}		10^{-5}
f		1.15
α		0.5
NT		100
j_{level}		6
h_{last}		10^{-5}

TABLE 6: Integral-Equation and Simulation Results for i_{max} in Linear-Sweep Voltammetry Experiment

$\log(\nu_A)$	integral-equation method			simulation		
	$\gamma = 3$	$\gamma = 10$	$\gamma = 21$	$\gamma = 3$	$\gamma = 10$	$\gamma = 21$
-2.00	5.45	7.88	10.2	5.45	7.86	10.14
-1.00	5.7	8.44	11.1	5.70	8.42	11.10
0.00	6.77	10.6	14.2	6.76	10.54	14.14
1.00	10.4	15.2	19.5	10.5	15.2	19.5
2.00	20	25.2	30.3	20.2	25.3	30.3
3.00	50	54.8	60	50.5	55.3	60.3
4.00	145	149	154	147	152	156
5.00	446	448	454	452	456	460
6.00	1400	1400	1400	1417	1421	1425

TABLE 7: Integral-Equation and Simulation Results for $\xi_{m/2}$ in Linear-Sweep Voltammetry Experiment

$\log(\nu_A)$	integral-equation method			simulation		
	$\gamma = 3$	$\gamma = 10$	$\gamma = 21$	$\gamma = 3$	$\gamma = 10$	$\gamma = 21$
-2.00	0.105	0.141	0.149	0.089	0.121	0.147
-1.00	0.255	0.314	0.344	0.246	0.297	0.320
0.00	0.564	0.542	0.449	0.518	0.467	0.420
1.00	0.703	0.599	0.524	0.713	0.593	0.534
2.00	0.904	0.790	0.719	0.914	0.809	0.736
3.00	1.020	0.962	0.921	1.029	0.983	0.939
4.00	1.063	1.037	1.022	1.073	1.055	1.040
5.00	1.078	1.063	1.060	1.086	1.081	1.077
6.00	1.090	1.080	1.068	1.091	1.089	1.087

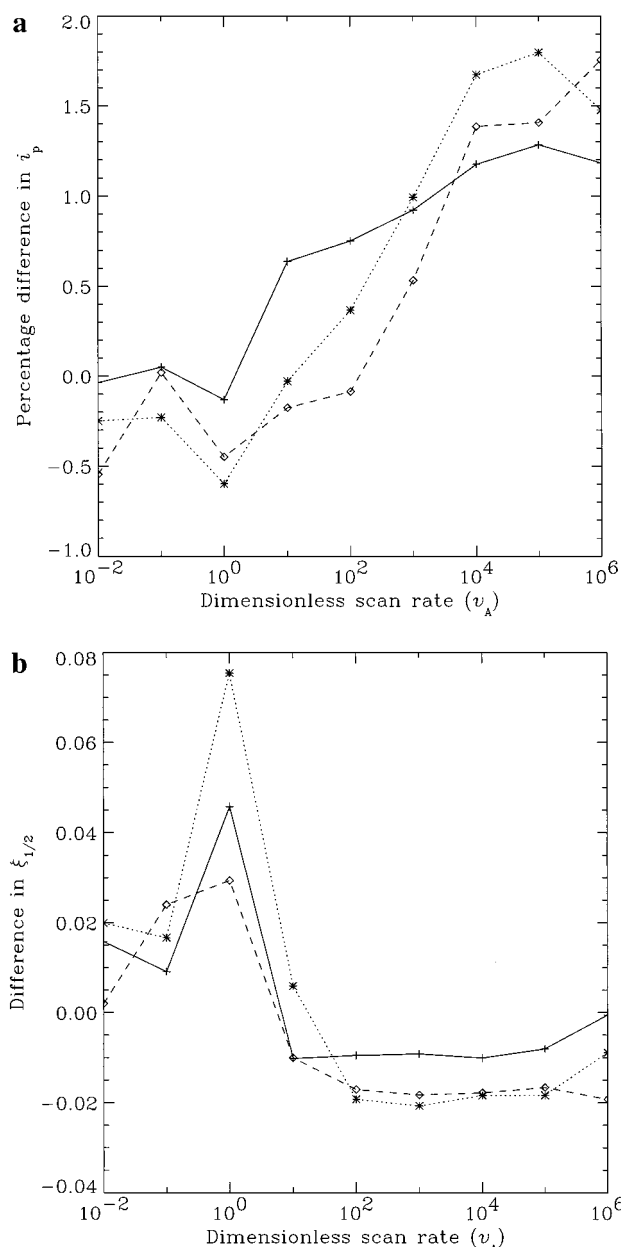
TABLE 8: Results of LSV Convergence Testing for Ring of Thickness $\gamma = 10.0$ at a Scan Rate of $\nu_A = 1.0$

h_{last}	f	NL	j_{level}	i_{max}	$\xi_{m/2}$
10^{-5}	1.15	100	2	10.5465	0.4468
		100	3	10.5385	0.4661
		100	4	10.5367	0.4671
		100	5	10.5371	0.4668
		100	6	10.5371	0.4666
10^{-5}	1.15	200	6	10.5287	0.465413
		400	6	10.5249	0.465358
10^{-5}	1.2	100	6	10.5515	0.4659
	1.25	100	6	10.5696	0.4656
10^{-6}	1.09	100	6	10.5575	0.4668

$\xi_{m/2}$, have been presented for ring thicknesses of $\gamma = 3.0, 10.0$, and 21.0 over 9 decades of the dimensionless scan rate, ν_A . The parameters, i_{max} , and ν_A are all nondimensionalized with respect to the ring area

$$i_{\text{max}} = \frac{I_{\text{max}}}{nFD[A]_{\text{bulk}}L} \quad (40)$$

$$\nu_A = \frac{nFvL^2}{DRT} \quad (41)$$

**Figure 8.** Discrepancy in i_{max} (a) and percentage difference in $\xi_{m/2}$ (b) between simulation and integral-equation results for $\gamma = 3$ (+), 10 (*), and 21 (◇).

where $L = (A/\pi)^{1/2}$. $\xi_{m/2}$ is also defined as

$$\xi_{m/2} = \frac{nF(E_{m/2} - E^{\circ'})}{RT} \quad (42)$$

Kalpathy et al. quoted an accuracy of $\pm 1\%$ for i_{lim} data and ± 0.008 in the dimensionless potential data. Wu et al.²⁹ used Szabo's empirical eq 4 to derive an integral equation that described the reversible electrode current. Results were illustrated for peak height and width at half-height for a variety of thicknesses ($\gamma = 0.5-20$) for dimensionless scan rates, $P < 20$. P is defined as

$$P = \left(\frac{nFv\omega^2}{RTD_A} \right)^{1/2} \quad (43)$$

where $\omega = R_b - R_a$. P is related to Tallman's dimensionless variables as $P = \sqrt{2\gamma\nu_A}$.

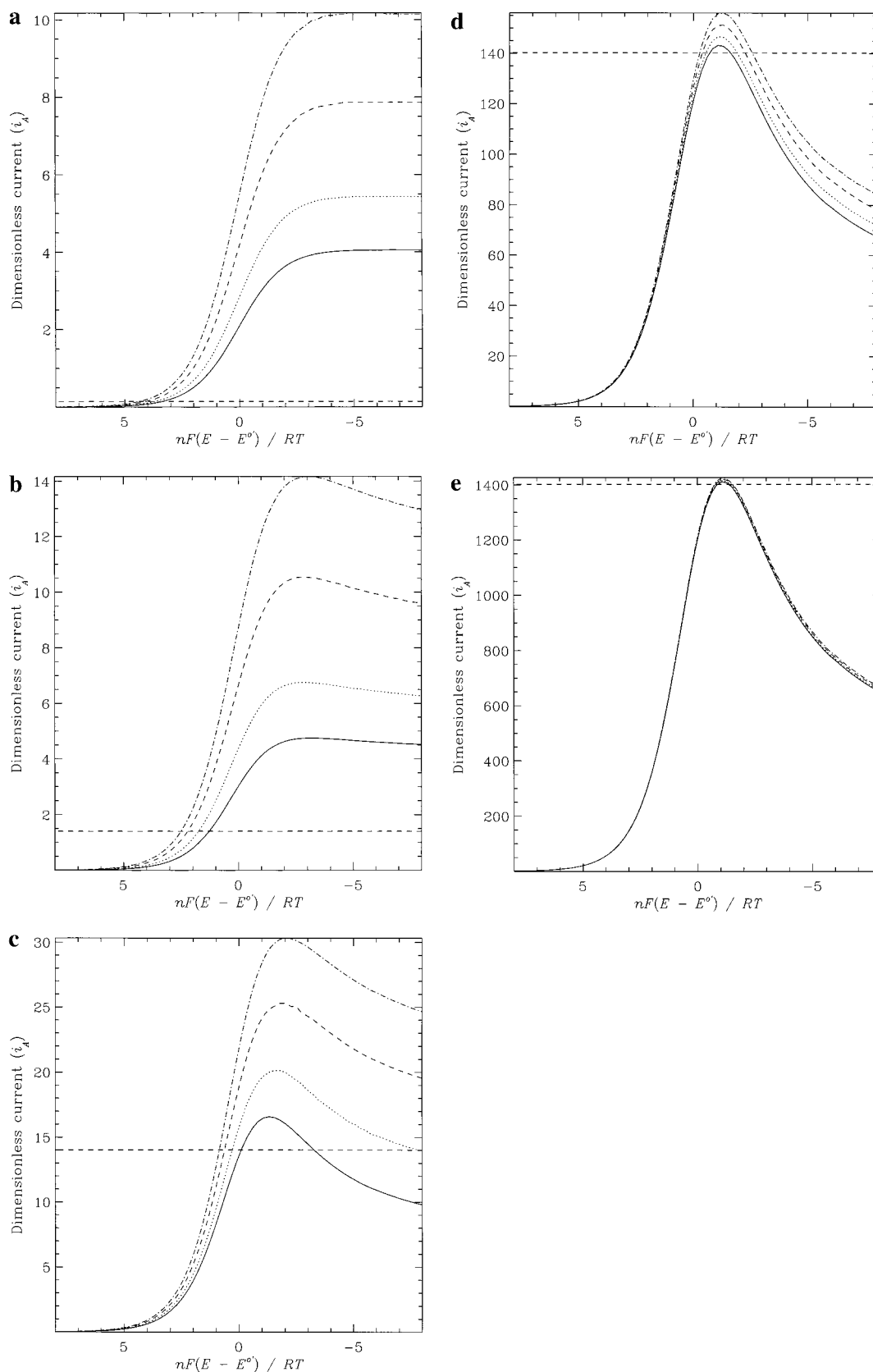


Figure 9. Voltammograms for the microdisk electrode (unbroken line) and microring electrode of thickness $\gamma = 3$ (dotted line), 10 (dashed line), and 21 (dotted and dashed line) for dimensionless scan rates of (a) 10^{-2} , (b) 10^0 , (c) 10^2 , (d) 10^4 , and (e) 10^6 . The straight dotted line indicates the peak height for pure linear diffusion.

Wu et al. also cite an approximate empirical analytical equation for the peak height applicable to values of $v_A \leq (2\gamma)^{-1}$. Simulations were run for rings of the same three thicknesses with the parameters given in Table 5. In all cases, a value of k_0

$= 10^{10} \text{ cm s}^{-1}$ was used, which is sufficiently large for the kinetics to be deemed reversible. Values of i_{max} and $\xi_{m/2}$ were computed by fitting a cubic spline to the voltammogram data. Resulting simulation data for i_{max} and $\xi_{m/2}$ are presented

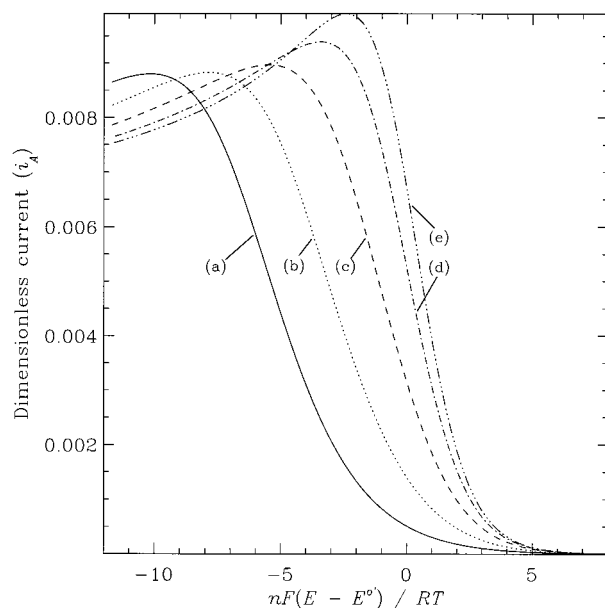


Figure 10. Results of linear-sweep voltammetry with quasi-reversible electrochemistry for $k^0 =$ (a) 10^{-2} , (b) 3.1×10^{-2} , (c) 10^{-1} , (d) 3.1×10^{-1} , and (e) 10^0 cm s^{-1} .

TABLE 9: Integral-Equation, Simulation, and Analytical Results for $\xi_{m/2}$ in Linear-Sweep Voltammetry Experiment at Microdisk Electrode

log(b)	$\xi_{m/2}$			errors in $\xi_{m/2}$ compared to analytical	
	simulation	integral-equation	analytical	simulation	integral-equation
-2.0	0.069	0.076	0.059	-0.010	0.017
-1.0	0.199	0.208	0.182	-0.017	0.026
0.0	0.493	0.508	0.489	-0.004	0.019
1.0	0.840	0.851	0.843	0.003	0.008
2.0	1.008	1.020	1.009	0.001	0.011
3.0	1.067	1.048	1.064	-0.003	-0.016
4.0	1.084	1.067	1.082	-0.002	-0.015
5.0	1.090	1.076	1.088	-0.002	-0.012
6.0	1.092	1.093	1.089	-0.002	0.004

alongside the results of Kalpathy et al. in Tables 6 and 7, respectively. The discrepancy of simulated data relative to previous integral-equation data is illustrated in Figure 8a,b. Figure 8a shows an increasing discrepancy between simulated and integral-equation results as we increase the scan rate from close to steady-state conditions ($\nu_A = 10^{-2}$) up to values at which linear diffusion dominates ($\nu_A = 10^6$). Errors are smaller than 1% for a large range of scan rates ($\nu_A = 10^{-2}$ to 10^3) and similar for all electrode thicknesses. We also notice that, up to scan rates of $\nu_A = 10^5$, numerical results presented in Table 6 are still more accurate than those calculated using linear diffusion approximations. Consideration of the errors in $\xi_{m/2}$ (calculated as the absolute difference between numerical and semiintegral results) illustrates a more complex behavior. Here, the error shows a definite peak at the dimensionless scan rate of unity, which is greatest for the ring with $\gamma = 10.0$. All data points to either side of the $\nu_A = 1$ data differ by not more than ± 0.02 . To test whether this was likely to be a numerical simulation problem, simulations were run first with increased numbers of time iterations, NL , second with different numbers of Richtmyer levels, j_{level} , and last with varying the value of the expansion parameter f on the mesh. We also apply the same calculation on a finer optimized mesh ($h_{\text{last}} = 10^{-6}$, $f = 1.09$). The results are tabulated in Table 8. The data show that none of the methods tested above leads to a significant change in the

values of $\xi_{m/2}$. Any convergence problems due to discretization errors in the finite difference techniques should be lessened by more time steps and finer meshing; however, this is evidently not the case. We therefore look to the likelihood that the errors are due to the approximations necessary in the formulation of the integral-equation methods. It is therefore of benefit to check the validity of the finite difference method and also the integral-equation method, applied to the microdisk problem, for which more reliable $\xi_{m/2}$ data is available. Simulations were therefore run according to the method laid out by Gavaghan.³⁰ For comparison, voltammograms for a reversible couple at a microdisk electrode and microring electrodes of thickness $\gamma = 3, 10$, and 21 are shown in Figure 9a–e. Analysis of the resulting data is made with reference to the analytical results of Aoki,³¹ whereby the half-peak potential for LSV at a microdisk electrode of radius R_d is

$$\xi_{m/2} = -0.694 \tan^{-1}(0.85p) \quad (44)$$

where p is

$$p = \left(\frac{nFR_d^2 \nu}{RTD} \right)^{1/2} \quad (45)$$

This equation was derived empirically by fitting elementary functions to analytic data. It is accurate to ± 0.016 in $\xi_{m/2}$. Table 9 details simulation results and compares the semiintegral and analytical results of Tallman and Aoki, respectively. As can be seen from Table 9, $\xi_{m/2}$ data for the simulation is closer to the empirical analytical result than to the semiintegral results. Moreover, at low values of ν_A (10^{-2} to 10^0), the errors for the simulation data and the integral-equation data are opposite in sign. Similar behavior in the ring electrode may indeed explain the large discrepancies in $\xi_{m/2}$ observed between simulated and integral-equation method linear-sweep voltammetry data. Finally, we should highlight that implementing the Butler–Volmer kinetics in the electrode boundary condition, rather than assuming reversibility, allows the investigation of the quasi-reversible electrochemical region. To illustrate this fact, linear-sweep voltammograms were run at a ring of $\gamma = 10.0$ for five logarithmically linear rate constants between 10^{-2} and 10^0 cm s^{-1} ($D = 10^{-5}$ $\text{cm}^2 \text{s}^{-1}$; $R_b = 10^{-3}$ cm). The voltammograms are illustrated in Figure 10.

Computational Methods. To solve eq 9, we employ the NAG library F11 (preconditioned Krylov subspace) methods.²⁵ In particular, we use an incomplete LU preconditioner ($L_{\text{FILL}} = 0$, $D_{\text{TOL}} = 10^{-14}$ (**F11ZAF**, **F11BAF**)) and the BICGSTAB ($l = 4$) (**F11DCF**) to solve the resulting linear system of equations. The simulation code was written in C++ and run on a Silicon Graphics Origin 2000 server. Simulation data was presented and interpreted using IDL 5.0. Cubic spline fitting and spline evaluation was performed on linear-sweep voltammogram data using NAG routines **E02BAF** and **E02BBF**. The fitting algorithm automatically placed ties at every fifth data point. Also, to increase accuracy around the current peak, the fitting was applied to the logarithm of the peak data and weighted as the square root of the current value at each point.

Conclusions

A method has been presented for finite difference numerical simulations at microring electrodes for a large range of thicknesses. Results have been gathered for steady-state voltammetry, chronoamperometry, and linear-sweep voltammetry and shown to be comparable, and in some cases, superior to other

methods. Results for chronoamperometry are shown to agree within $\pm 1\%$ with integral-equation methods over 4 decades of electrolysis time for rings of moderate thickness. For linear-sweep voltammetry, simulation peak current results for a reversible couple are shown to agree with integral-equation data to better than $\pm 1.5\%$. Moreover, new half-peak voltage data are presented. Because of the proliferation of literature on finite-difference techniques, the method presented here will be highly adaptable to more challenging electrochemical systems, for example, quasi-reversible linear-sweep voltammetry. The study of light-initiated reactions at the microoptical ring electrodes is a present area of investigation.

Glossary

R_a , cm	outside ring radius
R_b , cm	inside ring radius
r_a	normalized inside ring radius
r_{\max}	semiinfinite boundary length in r axis
z_{\max}	semiinfinite boundary length in z coordinate
I , A	current
t , s	time
T , K	temperature
E° , V	formal potential
k° , cm s ⁻¹	standard electrochemical rate constant
ν , V s ⁻¹	linear-sweep voltammetry scan rate
ν_A	dimensionless linear-sweep voltammetry scan rate
α	Butler–Volmer transfer coefficient
t_R, i_R	radius-normalized time/current
t_A, i_A	area-normalized time/current
$\xi_{m/2}$	dimensionless half-peak potential in linear-sweep voltammogram
i_{\max}	dimensionless peak current in linear-sweep voltammogram
l_0	Szabo ring parameter
γ	dimensionless perimeter-squared-to-area ratio as used by Tallman
a, b	concentration spatial functions
U_{ij}	discretized concentration solution at location z_i, r_j

k_j, h_i	mesh spacings in z and r directions.
NT	number of time iterations in simulation
h_{last}	mesh spacing adjacent to electrode edge
$f (f_{\text{opt}})$	mesh expansion factor (optimized)
δ	time-step expansion factor

References and Notes

- (1) Lee, Y.; Ameniya, S.; Bard, A. J. *Anal. Chem.* **2001**, 73, 2261.
- (2) Pennarun, G. I.; Boxall, C.; O'Hare, D. *Analyst* **1996**, 121, 1779.
- (3) Kuhn, L. S.; Weber, A.; Weber, S. G. *Anal. Chem.* **1990**, 62, 1631.
- (4) Zhung, Q.; Che, H. *Electroanalysis* **1994**, 6, 485.
- (5) Cohen, C. B.; Weber, S. G. *Anal. Chem.* **1993**, 65, 169.
- (6) Casillas, N.; James, P.; Smyrl, W. H. *J. Electrochem. Soc.* **1995**, 132, L16.
- (7) Symanski, J. S.; Bruckenstein, S. *J. Electrochem. Soc.* **1988**, 135, 1985.
- (8) Fleishmann, M.; Pons, S. *J. Electroanal. Chem.* **1987**, 222, 107.
- (9) Fleishmann, M.; Bandyopadhyay, S.; Pons, S. *J. Phys. Chem.* **1985**, 89, 5537.
- (10) Szabo, A. *J. Phys. Chem.* **1987**, 91, 3108.
- (11) Symanski, J. S.; Bruckenstein, S. *Extended abstract*, 165th Meeting of the Electrochemical Society, May 1984; Electrochemical Society: Pennington, NJ, 1984; p 527.
- (12) Smythe, W. R. *J. Appl. Phys.* **1951**, 22, 1499.
- (13) Philips, C. G.; Stone, H. A. *J. Electroanal. Chem.* **1995**, 396, 277.
- (14) Cope, D. K.; Tallman, D. E. *J. Electroanal. Chem.* **1991**, 303, 1.
- (15) Cope, D. K.; Scott, C. H.; Tallman, D. E. *J. Electroanal. Chem.* **1989**, 289, 49.
- (16) Kalpathy, U.; Tallman, D. E. *J. Electroanal. Chem.* **1992**, 325, 65.
- (17) Tallman, D. E. *Anal. Chem.* **1994**, 66, 557.
- (18) Gavaghan, D. J. *J. Electroanal. Chem.* **1998**, 456, 1.
- (19) Saito, Y. *Rev. Polarogr.* **1968**, 15, 177.
- (20) Compton, R. G.; Dryfe, R. A. W.; Wellington, R. G.; Hirst, J. *J. Electroanal. Chem.* **1995**, 383, 105.
- (21) Shoup, D.; Szabo, A. *J. Electroanal. Chem.* **1984**, 160, 1.
- (22) Heinze, J. *J. Electroanal. Chem.* **1981**, 124, 73.
- (23) Cooke, J. C. *Q. J. Appl. Math.* **1963**, 16, 193.
- (24) Whiteman, J. R.; Webb, J. C. *Bit. Nord. Tidskr. Informationsbe-handl.* **1970**, 10, 366.
- (25) Alden, J. A.; Compton, R. G. *J. Phys. Chem. B* **1997**, 101, 9741.
- (26) Wu, Z.; Zhang, Z. *Acta Chim. Sin.* **1993**, 51, 239.
- (27) Oldham, K. B. *J. Electroanal. Chem.* **1981**, 122, 1.
- (28) Feldberg, S. W.; Goldstein, C. I. *J. Electroanal. Chem.* **1995**, 397, 1.
- (29) Wu, Z.; Zhang, Z. *Acta Chim. Sin.* **1993**, 51, 697.
- (30) Gavaghan, D. J. *J. Electroanal. Chem.* **1998**, 456, 25.
- (31) Aoki, K.; Akimoto, K.; Tudoka, K.; Matsuda, A.; Osteryoung, J. *J. Electroanal. Chem.* **1984**, 171, 21.